Development of a Model for Irradiation-Assisted Grain Growth for Nanocrystalline UO$_2$

Md Ali Muntaha[a], Larry K. Aagesen[b], Michael R. Tonks[c,*]

[a]*Fuel Development Performance and Qualification, Idaho National Laboratory, Idaho Falls, ID 83415, USA*
[b]*Computational Mechanics and Materials, Idaho National Laboratory, Idaho Falls, ID 83415, USA*
[c]*Department of Materials Science and Engineering, University of Florida, Gainesville, FL 32611, USA*

Abstract

In this work, we have developed a model for irradiation-assisted grain growth in nanocrystalline UO$_2$ using the MARMOT code. We include the impact of irradiation on UO$_2$ grain growth by coupling a phase field grain growth model with a heat conduction simulation that features a random heat source representing thermal spikes. Our model parameters have been calibrated against experimental measurements at 300 K. The calibrated model predicts grain growth in an irradiated UO$_2$ thin film that compares well with experimental data at 50 K. These results suggest that thermal spikes are the major cause of the irradiation-assisted grain growth observed in the UO$_2$ experiments. They also indicate that irradiation-assisted grain growth is only significant with average grain sizes less than 35 nm, and thus can be neglected when considering fuel performance of typical UO$_2$ fuel pellets.

Keywords: Phase field modeling, Irradiation, Grain growth, Multiphysics coupling

[*]Corresponding author
Email address: `michael.tonks@ufl.edu` (Michael R. Tonks)

1. Introduction

Grain growth occurs in polycrystalline materials to reduce their total free energy [1]. Various driving forces, such as a reduction in grain boundary (GB) energy, stored elastic energy, and stored defect energy, contribute to grain growth [2]. The reduction of GB energy decreases the total area of GBs, which have a higher energy compared to the interior of the grains. The process involves the growth of larger grains and the disappearance of smaller ones, causing a decrease in the number of grains and an increase in the average grain size. The kinetics of grain growth are typically defined by the GB mobility, which often has an Arrhenius dependence on the temperature. Thus, grain growth typically occurs only at elevated temperatures, especially in ceramics such as UO_2 [3–6].

However, radiation can induce grain growth at much lower temperatures than is necessary for thermally-activated grain growth [7–14], including cryogenic temperatures. For example, Kaoumi et al. showed accelerated grain growth in ion-irradiated metallic thin films of Zr, Cu, Pt, and Au [7], and supersaturated solid solutions of ZrFe and CuFe [8]. Later, Yu et al. [12] showed irradiation-accelerated grain growth for in-situ ion-irradiated UO_2 thin films. Kaoumi et al. [7] developed an analytical model that predicted the evolution of the average grain size in irradiated materials based on the direct impact of thermal spikes on GBs, which accelerated curvature-driven growth. Bufford et al. [11] developed a mesoscale model of grain growth in which they introduced randomly distributed regions of locally increased GB mobility and compared the predictions with data from in situ ion irradiations of Au thin films.

The grain size of UO_2 reactor fuel influences its performance by directly affecting the fission gas release, heat conduction, creep, and fracture [15–26]. For this reason, a large number of experiments [27] and atomistic [28, 29] and mesoscale simulations [4, 30–34] have been carried out to investigate GB migration and grain growth in UO_2, as summarized by Tonks et al. [3]. However, these studies have focused on thermally-driven GB migration and have not considered irradiation-assisted grain growth. Therefore, there is a need to develop models that consider irradiation-assisted grain growth in UO_2 to determine if it has a significant impact on fuel performance.

In this work, we have included irradiation-assisted grain growth in a phase field grain growth model for UO_2. We have compared the predictions of the model with the in situ grain growth data from the irradiation experiments carried out by Yu et al. [12] in UO_2 thin films. We begin by summarizing the experimental data from Yu et al. in Section 2. We discuss the model formulation in Section 3, including the grain growth and heat conduction models, the numerical methods, and the domain size

and parameter selection. In Section 4, we present results and we discuss them in Section 5. Finally, we conclude in Section 6.

2. Experimental observation of irradiation assisted grain growth in UO_2

In the range of cryogenic to room temperatures, the migration of GBs under irradiation is generally assumed to be associated with the thermal spikes that take place during the process of radiation-induced damage. When an energetic particle strikes a target material, the kinetic energy of the particle is deposited into a target atom. This transfer of energy takes the target atom to a high-energy state, making it mobile and displacing it in the lattice. These displaced atoms can, in turn, collide with other atoms in the lattice, creating a chain reaction of collisions, which is called the collision cascade. When a high-energy ion, e.g. an energy $\geq 5.42 \times 10^{12}$ eV/nm^{3}s [13], impacts a material surface, an extremely high-energy thermal spike event is created, which lasts for picoseconds [12, 13]. When a thermal spike occurs at or near a GB, it incites an increase in the number of atomic displacements across the boundary. This action results in a movement of the GB, which ultimately leads to accelerated grain growth.

Yu et al. [12] used in situ ion irradiation to investigate irradiation-assisted grain growth in UO_2. They performed isothermal irradiation experiments on UO_2 thin films (50 nm thickness) using 1 MeV Kr^{2+} ions at a flux of 6.25×10^{15} ions/m^{2}s, reaching a maximum fluence of 7×10^{19} ions/m^2. The irradiations were carried out for approximately 3 hours at temperatures ranging from 50 K to 1075 K. Yu et al. [12] measured the grain diameter using transmission electron microscopy (TEM) images that were collected by stopping the irradiations at regular intervals. Details on how the grain diameter was collected are available in their paper [12]. For all temperatures, grain growth occurred rapidly in the early stages and then slowed significantly over time, as shown in Fig. 1. The average thermal spike energy q_c and the number of thermal spikes per ion χ were calculated using the Stopping and Ranging of Ions in Matter (SRIM) code [35].

To determine the temperatures at which thermally activated grain growth is significant in their irradiated samples, Yu et al. [12] also carried out grain growth experiments at the same temperatures without irradiation. They observed no thermally activated grain growth after a 5-hour annealing period for temperatures up to 475 K. Thus, only irradiation-assisted grain growth was significant in 50 K, 300 K and 475 K irradiations (see Fig. 1). Thermally-activated grain growth did occur above 475 K, indicating that both thermally-activated and irradiation-assisted grain growth were significant
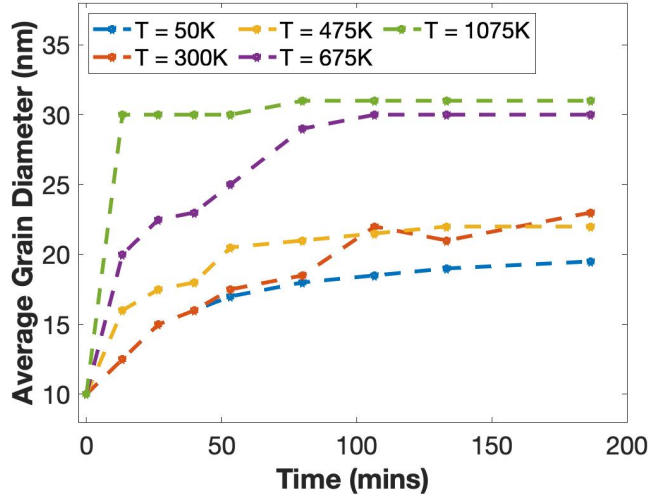
Fig. 1 The average grain diameter versus time from in situ ion irradiations of UO_2 nanocrystallien thin films carried out by Yu et al. [12] at various temperatures. The time was computed by dividing the reported fluences by the irradiation flux.

in the 675 K and 1075 K irradiations. Yu et al. [12] also found that the thermal spike diameter was temperature dependent for $T > 300$ K, with larger diameters observed at higher bulk material temperatures. Due to these results, we focus on modeling the behavior at temperatures of 300 K and below, where we can assume that the spike diameter is independent of temperature and that thermally activated grain growth is negligible.

3. Model development

We have developed a mesoscale model of irradiation-assisted grain by coupling a phase field grain growth model with a heat conduction model that includes heat generation due to thermal spikes arising from collision cascade events. In this section, we summarize the model and include all the assumptions involved in its development. We begin by summarizing the phase field grain growth model and the heat conduction model. We then discuss its numerical implementation and the parameter selection.

3.1. Phase field grain growth model

In phase field grain growth models, instead of tracking the precise location of sharp GBs, the phase field method represents the grain structure using smooth, continuous field variables η_i, called order parameters. A specific order parameter $\eta_i = 1$ in grain i, $\eta_i = 0$ in all other grains $j \neq i$, and $0 < \eta_i < 1$ across GBs between grain i and other grains. The order parameters describing the grains evolve to

4

minimize the free energy of the system according to the Allen-Cahn equation

$$\frac{\partial \eta_i}{\partial t} = -L \frac{\delta F}{\delta \eta_i}, \text{ for } i = 1, ..., N, \tag{1}$$

where N is the total number of order parameters, L is the order parameter mobility, F is the free energy functional, and $\frac{\delta}{\delta \eta_i}$ represents the variational derivative with respect to η_i. We use the phase field model developed by Moelans et al. [36], in which the free energy functional is

$$F = \int_V \left(\sum_i^N m \left(\frac{\eta_i^4}{4} - \frac{\eta_i^2}{2} + \frac{3}{2} \sum_i^N \sum_{j>i}^N \eta_i^2 \eta_j^2 + \frac{1}{4} \right) + \frac{\kappa}{2} \sum_i^N |\nabla \eta_i|^2 \right) dV, \tag{2}$$

where m and κ are model parameters that define the GB energy of the material and the width of the diffuse interfaces used to represent the GBs. Moelans et al. [36] developed quantitative expressions that define m, κ, and L in terms of the interface width l_{int}, GB energy γ, and the GB mobility M_{GB}:

$$m = 6 \frac{\gamma}{l_{int}} \tag{3}$$

$$\kappa = \frac{3}{4} \gamma l_{int} \tag{4}$$

$$L = \frac{4}{3} \frac{M_{GB}}{l_{int}}. \tag{5}$$

In our model, we assume all GB types have the same energy and mobility. Expressions for the average GB energy and mobility for UO$_2$ are presented by Tonks et al. [37]. The average GB energy is a function of temperature according to

$$\gamma = \left(1.56 - 5.87 \times 10^{-4} T\right) \text{ J/m}^2. \tag{6}$$

The average GB mobility follows the standard Arrhenius expression

$$M_{GB} = M_{GB}^0 e^{-\frac{E_a}{RT}}, \tag{7}$$

where $M_{GB}^0 = 2.14 \times 10^{-7}$ m^4/(J s) is the prefactor, $E_a = 290$ kJ/mol is the activation energy, R is the ideal gas constant constant, and T is the temperature. We assume that the GB mobility is defined by this expression even for regions within the thermal spike that can locally reach above the melting temperature.

3.2. Heat conduction model

To model irradiation-assisted grain growth, we have to modify the phase field grain growth model to include the impact of thermal spikes due to collision cascades on GB migration. The idea of a thermal spike in a material has been confirmed by analytical models and molecular dynamics simulations [38]. Bufford et al. [11] developed a phase field grain growth model that included the impact of thermal spikes by increasing the GB mobility in randomly selected regions representing the thermal spike. They showed that this approach resulted in predicted grain growth behavior that was qualitatively similar to that observed in radiation experiments. In our model, we couple the grain growth equations to a heat conduction equation that includes randomly distributed regions of short-lived heat generation, which elevate the local temperature, often above the melting point, for a short period of time.

We solve for the change in the temperature field T with time t across the polycrystal by solving the heat equation:

$$\rho c_p \frac{\partial T}{\partial t} = \nabla \cdot k \nabla T + Q, \tag{8}$$

where ρ is the density, c_p is the specific heat, k is the thermal conductivity, and Q is the heat generation due to thermal spikes.

The heat generation field Q varies stochastically in space across the domain and in time due to the random nature of thermal spikes from cascades occurring in the system. A given rate of cascades per unit volume per unit time, P_c, was used to calculate the probability of a cascade occurring. It is a function of the radiation flux ϕ according to

$$P_c = \chi \phi, \tag{9}$$

where χ is the number of cascades generated per ion per unit length. When a cascade is randomly determined to occur during a certain time step, the center location of the cascade is randomly determined from a uniform distribution. The value of Q is then non-zero in a spherical region of radius r_s around the center point for a specific thermal spike duration t_s of the order of picoseconds. The magnitude of the heat generation rate within the spherical region is

$$Q = \frac{q_s}{V_s t_s}, \tag{10}$$

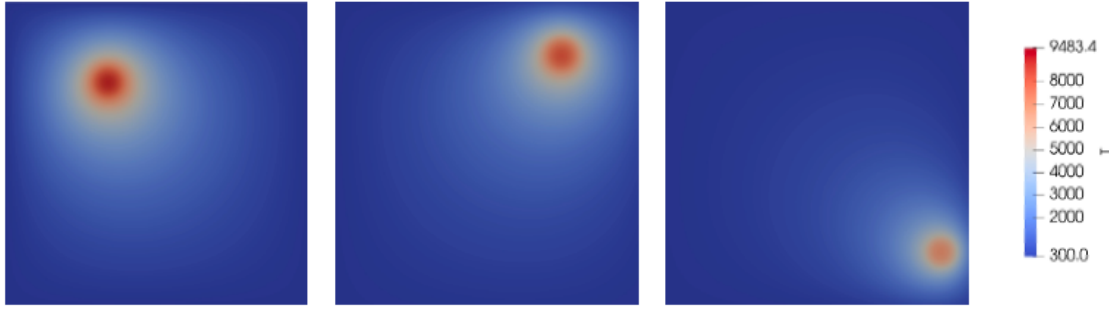where q_s is the average thermal spike energy in eV per spike and $V_s = 4/3\ \pi r_s^3$ is the spike volume.

Fig. 2 Demonstration of the implementation of thermal spike events using the heat conduction model for a domain size of 100 nm × 100 nm. Temperature profiles are displayed at three different time steps, where thermal spike events can be observed at three different random locations, each with the peak temperatures at the center of the spikes.

The local heat generation due to thermal spikes results in local increases in temperature that can increase well above the melting temperature of UO_2, as demonstrated in Fig. 2. For this demonstration, the initial temperature is 300 K in a 100 nm × 100 nm domain. We assume Dirichlet boundary conditions of 300 K on all boundaries to represent heat transport from the sample boundaries that are in contact with the environment. The temperature rises as high as 9483.4K at the center of a thermal spike. After the spike duration, the heat quickly dissipates through the material and the local temperature returns to room temperature.

3.3. Domain Size and Parameter Selection

To simulate the ion irradiations from Yu et al. [12], we use 2D simulations with a square domain. We use 2D simulations rather than 3D to reduce the computational cost. We assume an initial average grain size of 10 nm, which is consistent with the average grain sizes from the experimental thin films. We assume columnar grains, such that the grain structure does not change through the thickness of the films. We also assume no heat transport from the top and bottom of the films and that the thermal spikes are cylinders rather than spheres. Together, these assumptions result in the grain growth not changing in the z-diretion, allowing us to model irradiation-assisted grain growth in 2D. We assume a domain thickness in the z-direction of $4/3r_s$, such that volume of the thermal spike cylinder in our 2D domain is equivalent to the thermal spike sphere in a 3D domain.

Using a domain size as large as the actual thin films in the experiments would result in too many grains to be computationally feasible. Therefore, we select a smaller domain size to provide a more reasonable number of grains. We use a 710 nm by 710 nm domain with 5000 initial grains. The
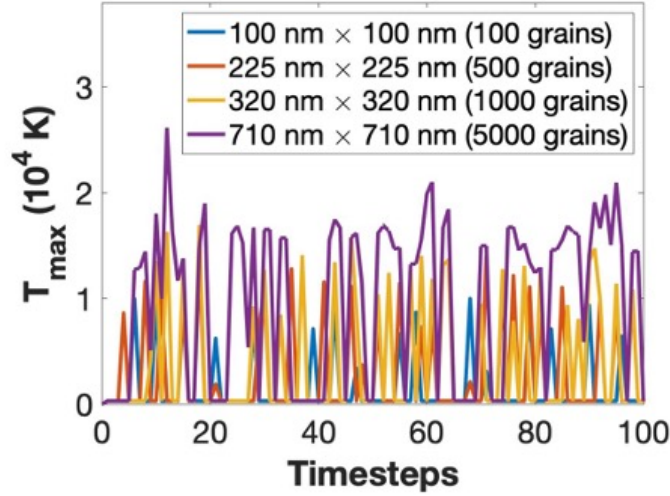
7

Fig. 3 Demonstration of the peak temperatures over time for different domain sizes. The legend also indicates the number of initial grains that can be accommodated in that domain with an average grain size of 10 nm.

grain structure is constructed from a Voronoi tessellation and then thermally-activated grain growth is simulated to obtain a more realistic 5000 grain structure.

Natural boundary conditions are used for the order parameters η_i. For the temperature, heat is removed from the system at the sample edges by the holder. Thus, we apply Dirichlet boundary conditions at all boundaries with a value of the irradiation temperature. However, due to the temperature boundary conditions, the peak temperatures that occur vary with the domain size, as shown in Fig. 3. The smaller the domain size, the more the boundary conditions reduce the maximum temperatures during a thermal spike. Thus, it is desirable to use as large a domain size as is computationally feasible. We find that the 710 nm by 710 nm square domain provides the best balance between computational expense and accuracy.

All of the parameters for our simulations are either taken from the literature for UO_2 or are chosen to represent the ion irradiation experiments from Yu et al. [12]. All of the properties used in the model can be found in Table 1, including the references where the values were obtained.

To represent the ion irradiation conditions from Yu et al. [12], we use the ion flux applied in their work, $\phi = 6.25 \times 10^{12}$ ions/cm²s. We use a thermal spike radius $r_s = 4.84$ nm and an average spike energy $q_c = 25.65$ keV, as described in the experimental work [12]. The thermal spike duration t_s is unknown, but potentially ranges from around one to hundreds of ps. We determine the spike duration by comparing with the experiments, as discussed in Section 4.

8

Table 1: The parameter values used in our irradiation-assisted grain growth model. The reference that is the source of the value is provided, where applicable.

Parameter	Symbol	Value	Reference
Spike radius	r_s	4.84 nm	[7, 39]
Spike duration	t_s	1-100 ps	[40, 41]
Average thermal spike energy	q_s	25.65 KeV	[7, 39]
Thermal spike generated per ion per length	χ	0.0405 spikes/ion-nm	[7, 39]
Ion flux	ϕ	6.25×10^{11} ions/cm^2-s	[13]
Initial average grain size		10 nm	[12, 13]
Incident ion energy/type		1 MeV Kr	[12, 13]
Irradiation fluence		0 to 7×10^{19} ions/m^2	[12, 13]
Interfacial width	l_{int}	2 nm	
Thermal conductivity	k	3 W/m-k	[42–52]
Molar heat capacity	C_o	213.955 J/mol-k	[51–59]
UO$_2$ specific heat	C_p	0.7925 J/g-K	[13]
GB mobility prefactor	M_o	2.14×10^{-7} m^4/J-s	[3]
Activation energy	E_a	3 eV	[3]
GB energy	σ_{GB}	Eq. (6)	[37]
UO$_2$ density	ρ_{UO_2}	10.97 g/cm^3	
UO$_2$ molar mass		0.27 kg/mol	

3.4. Numerical Implementation

We implement our irradiation-assisted grain growth model using the finite element method in the mesoscale nuclear materials tool MARMOT [60], which is based on the Multiphysics Object-Oriented Simulation Environment (MOOSE) framework [61]. We use implicit time integration with a second-order backward Euler scheme to simultaneously solve Eq. (1) to evolve each of the order parameters η_i and Eq. (8) to evolve the temperature T.

To reduce the computational cost of polycrystal grain growth simulations, each order parameter represents multiple grains. We use the GrainTracker algorithm in MOOSE [62] to remap grains to new order parameters to avoid unphysical grain coalescence. We use 11 order parameters to represent all of the grains.

We solve the resultant system of nonlinear equations using the Preconditioned Jacobian Free Newton Krylov (PJFNK) method. Our nonlinear solution converges with a relative tolerance of 10^{-8} and an absolute tolerance of 10^{-10}. We have utilized MOOSE's automatic scaling feature to address the substantial variation in the magnitude of the order parameter and temperature residuals.

We use square elements to discretize the domain. The side length of the elements needs to be small enough to adequately resolve the interfacial width of 2 nm (see Table 1). We compare the predicted grain growth using element side lengths of 0.6 nm and 1.2 nm for a range of different spike rate cases, and find little difference in the predicted behavior as shown in in Fig. 4. Therefore, we use the larger element size of 1.2 nm to reduce the computational cost.
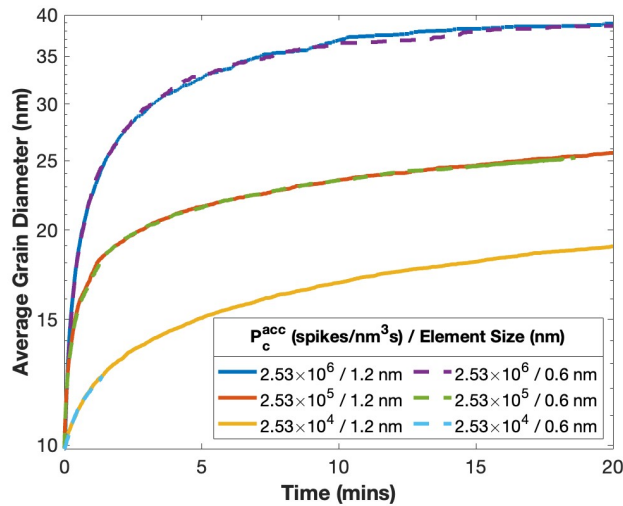

Fig. 4 Comparison of the predicted grain growth using an element size of 0.6 nm (shown with dashed lines) and 1.2 nm (shown with solid lines).

To further reduce the computational expense, we use adaptive time stepping. The time step adapts to maintain a target of 10 nonlinear iterations in the PJFNK solve per time step. When a thermal spike occurs, the time step automatically decreases to the spike duration t_s, to ensure that it is accurately represented. This connection between thermal spike events and the time step size is illustrated in Fig. 5.
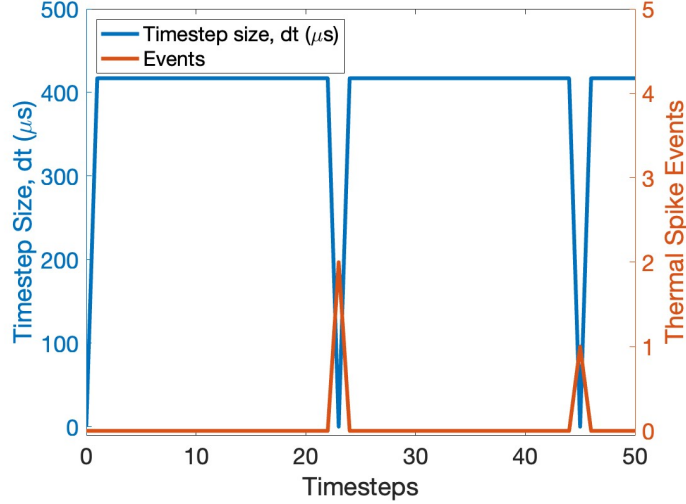

Fig. 5 Demonstration of the decrease in the time step during a thermal spike.

Even with adaptive time stepping, the requirement to resolve the spike duration makes the computational cost of the simulations unreasonably high. Assuming $\chi = 0.0405$ spikes per ion per nm [7, 39] and our ion flux, Eq. (9) gives a value of $P_c = 0.00253$ spikes/nm^{3}s. Given our 710 nm by 710 nm domain size with an assumed thickness of $4/3r_s$, this means on average a thermal spike will occur every 0.15 ms. Since our time step size goes down to the spike duration (1-100 ps) during each thermal spike there could be millions of time steps between each thermal spike. However,3 since the temperature is too low between thermal spikes to have any GB migration, the GBs only migrate during thermal spikes. Thus, we can reduce the computational cost by not modeling the time between thermal spikes and still accurately capture the irradiation-assisted grain growth.

To avoid modeling the time between thermal spikes, we increase the cascade rate P_c to the point where only one or two thermal spikes occur every time step. We then scale the time by the ratio of

the rates, where the actual time can be computed from the accelerated time:

$$\frac{P_c^{act}}{P_c^{acc}} = \frac{t_{acc}}{t_{act}}$$
$$t_{act} = \frac{P_c^{acc}}{P_c^{act}} t_{acc}, \tag{11}$$

where P_c^{act} and t_{act} are the actual rate and time and P_c^{acc} and t_{acc} are the accelerated rate and time. This approach is valid if only one spike occurs per time step or if multiple spikes occur but are far enough apart that they do not interact.

Preliminary results with different rate values and assuming a spike duration $t_s = 100$ ps are shown in Fig. 6. Each simulation was carried out using 160 processors on the University of Florida HiperGator supercomputer. The computational walltime is excessively high when considering the actual rate of 0.00253 spikes/nm^{3}s, as shown in Fig. 6a. It took around 300 hours to model 0.5 minutes and at least 12 minutes needs to be modeled to reach the first experimental data point. However, with an accelerated rate, the computational walltime decreases significantly. Increasing P_c by 10^7 ($P_c^{acc} = 2.53 \times 10^4$ spikes/nm^{3}s) reduces the computational walltime to model 0.5 minutes to around 10 hours. Increasing it by 10^9 reduces walltime to around 1 hour ($P_c^{acc} = 2.53 \times 10^6$ spikes/nm^{3}s).

The predicted change in the average grain diameter with time, shown in Fig. 6b, decreases slightly with probability $P_c^{acc} \leq 2.53 \times 10^4$ spikes/nm^3 s, possibly due to stochastic changes in the spike locations. However, it increases significantly with larger probabilities. This is because with $P_c^{acc} = 2.53 \times 10^4$ spikes/nm^{3}s, there is an average of 1.3 thermal spikes per time step. For larger probabilities, there are multiple thermal spikes per time step, and interaction between them raises the temperature and accelerates grain growth. This confirms that using an accelerated rate does not significantly impact the results as long as there are no multiple interacting thermal spikes in each time step. Hence, we use $P_c^{acc} = 2.53 \times 10^4$ spikes/nm^{3}s in our model and use Eq. (11) to calculate the actual time. Note that simulations with this P_c^{acc} are still computationally expensive, requiring 30 hours to simulate just 2 minutes of simulation time, but they are feasible to carry out.

4. Results

We apply our irradiation-assisted grain growth model to predict the evolution in a 710 nm by 710 nm domain with 5000 initial grains that is undergoing irradiation at 300 K. The grain growth is modeled for 40.5 minutes, assuming a thermal spike duration of 100 ps. The simulation takes 969.24
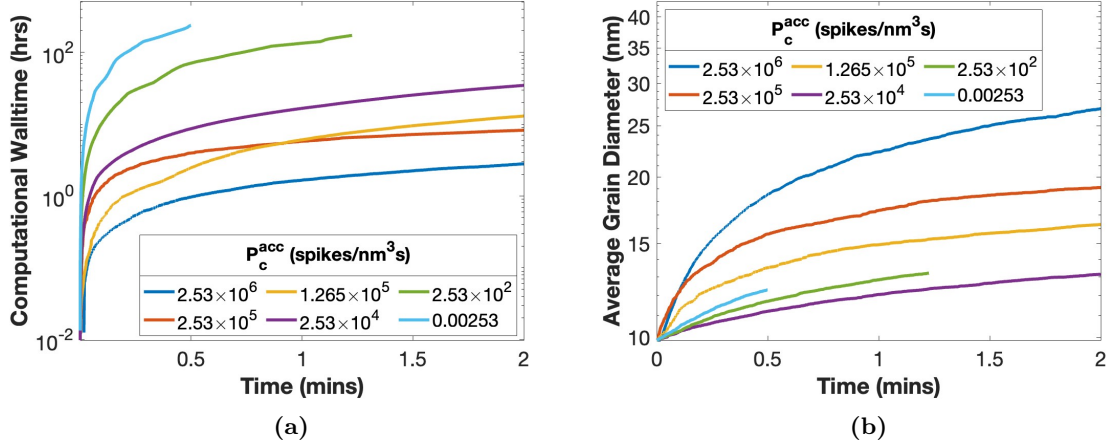
(a)

(b)

Fig. 6 Impact of P_c^{acc} on (a) the wall time and (b) the average grain diameter with time. The results use a 710 nm by 710 nm domain with $t_s = 100$ ps.
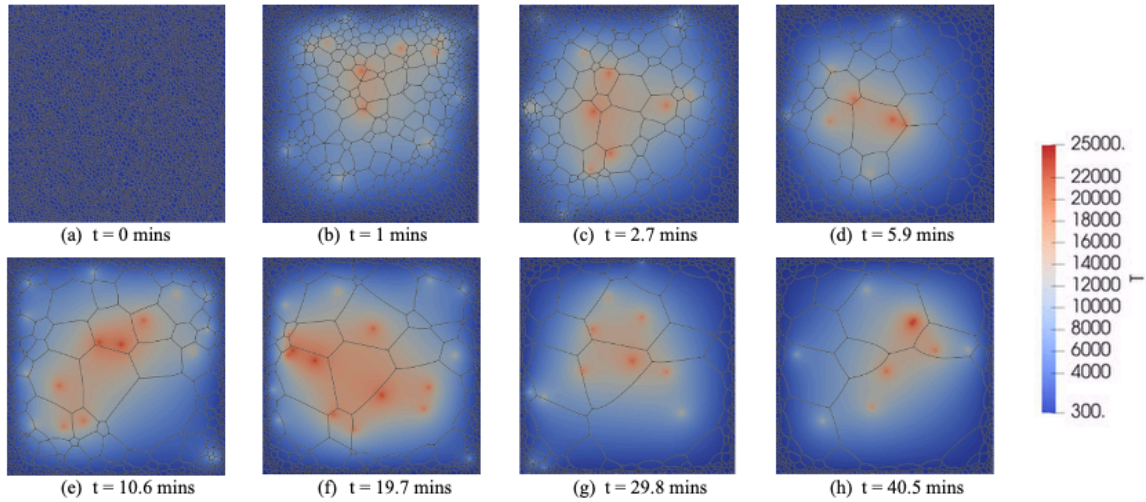

(a) t = 0 mins   (b) t = 1 mins   (c) t = 2.7 mins   (d) t = 5.9 mins

(e) t = 10.6 mins   (f) t = 19.7 mins   (g) t = 29.8 mins   (h) t = 40.5 mins

Fig. 7 Results from 2D simulations of irradiation-assisted grain growth at 300 K assuming a spike duration of $t_s = 100$ ps in a 710×710 nm UO_2 thin film with 5000 initial grains. Images of the polycrystal domain at different times are shown in (a) - (h). The images are shaded by the temperature in K and the GBs are shown in black.

13

hours (40.38 days) to complete on 160 processors. Images of the polycrystal at various times during the 40.5 minute irradiation are shown in Fig. 7. Due to the presence of thermal spikes, large gradients in temperature occur. The temperature is very high at the center of a spike, up to 25,000 K, but rapidly decreases moving outward from the center. These maximum temperatures are much higher than the melting temperature, but only remain so for a few time steps. The temperatures are higher for thermal spikes near the center of the domain than near the boundary due to the heat flux out of the boundary keeping the temperature at 300 K. These high local temperatures result in localized bursts of grain growth near the thermal spikes. Thus, the grains in the center of the domain grow very quickly, while the grains at the boundaries grow more slowly due to the low temperatures.

In the initial stages, the grains grow rapidly due to the numerous thermal spikes hitting at or near the GBs. These events result in significant boundary movement at the initial stage of the simulation, such as $t = 1$, 2.7, and 5.9 minutes in Fig. 7. However, at later stages of the simulation, such as $t = 29.8$, 40.5 minutes, fewer GBs are being hit by thermal spike events. Consequently, the growth rate slows in these later stages.

Figure 8 shows the average grain diameter with time from our simulation that assumes a spike duration of 100 ps. The average grain diameter quickly increases, especially compared to the results from a simulation at the same temperature but without irradiation, which shows no change in grain size. The growth rate predicted by our simulations with a 100 ps spike duration is significantly higher than was observed in Yu et al.'s experiments [12], even considering the uncertainty in the simulation results. However, as was mentioned in Section 3.3, we do not know the correct value for the spike duration. Therefore, we use the spike duration value to fit the modeling prediction with the 300 K experimental data.

We carry out simulations with spike durations ranging from 100 to 500 ps. To conserve computational time, we only simulate the full 60 min with the smallest (100 ps) and largest (500 ps) spike durations, and then simulate shorter times for the intermediate values. Note that the computational expense decreases with increasing spike duration, since the minimum time step size is equal to the spike duration. The grain growth decreases significantly with increasing spike duration, as shown in Fig. 9. This occurs because the magnitude of the heat generation goes down with increasing spike duration as shown in Eq. (10). Spike durations ranging from 150 to 250 ps result in growth behavior within the uncertainty ranges of the experiments. A spike duration of 200 ps results in the the best fit with the experimental data.
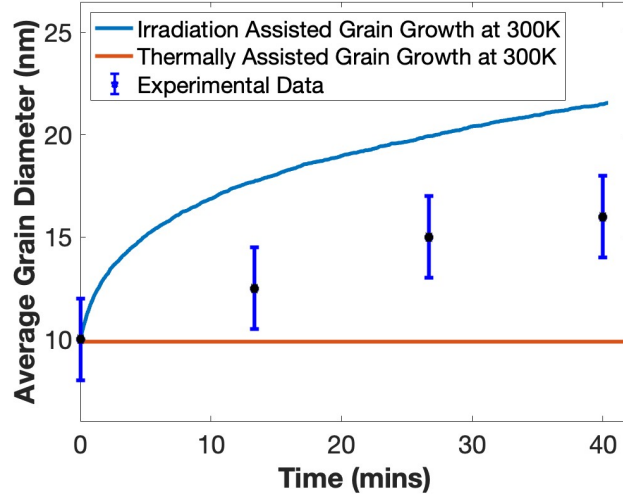
Fig. 8 Grain diameter versus time with a spike duration of $t_s = 100$ ps at 300 K. Simulation results with no irradiation and the experimental data [12] are also shown.
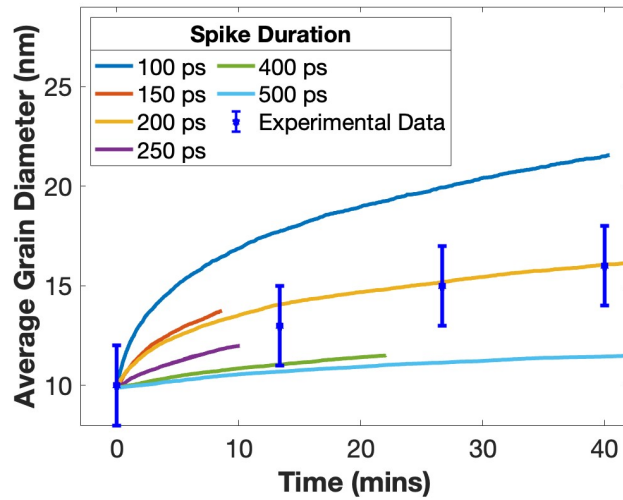

Fig. 9 Average grain diameter versus time at 300 K for spike durations ranging from 100 ps to 500 ps. The experimental data [12] are shown for reference.

15

Having determined a spike duration for which our results compare well with the data at 300 K, we now use it to model the grain growth at 50 K. The predicted average grain diameters versus time at 50 K are shown in Fig. 10, along with the corresponding experimental data. In addition to the simulation results, we include the analytical prediction based on the rate theory relation $D^n - D_n^3 = K\phi t$, where experimental analysis at 50 K has shown that the kinetics are well represented by $n = 3$ [12]. We therefore plot the analytical curve corresponding to $n = 3$, for which we obtain $K = 2.0258 \times 10^{-16}$ nm^3/(ions/m^2), in close agreement with the value $K = 9.64 \times 10^{-17}$ nm^3/(ions/m^2) reported in Ref. [12]. To obtain a best-fit curve for the 50 K data, we consider a generalized grain growth law of the form $D^n - D_0^n = K\phi t$, with an initial grain diameter $D_0 = 10$ nm and a constant ion flux $\phi = 6.25 \times 10^{15}$ ions m^{-2} s^{-1}. The parameters K and n are determined by minimizing the sum of squared differences between the model prediction and the experimental average grain diameters at 50 K using the Nelder–Mead simplex nonlinear least-squares method, which yields $n = 6.54$ and $K = 4.50 \times 10^{-12}$ nm^n (ions/m^2)$^{-1}$. This defines the best-fit curve shown in Fig. 10. The evolution of the grain diameter with time at 50 K is slightly slower than at 300 K. The temperature at the outer boundary is much lower, but the thermal spike temperatures driving the accelerated grain growth are still very high, resulting in the grain growth rate being nearly athermal. Overall, the simulation results, together with the analytical $n = 3$ rate-theory curve, show good agreement with the experimental measurements at 50 K. The consistency among these different representations provides additional validation that the model accurately captures the irradiation-induced grain-growth kinetics at lower temperatures (e.g. 50 K) for nanocrystalline UO_2.

5. Discussion

This model represents a large step forward in modeling irradiation-assisted grain growth. However, several assumptions and approximations were made in the simulations and it is important to consider their impact on the predicted behavior. First, we have assumed that the grain structure in the thin film samples is columnar, i.e., it doesn't change through the thickness of the film. This assumption enabled us to model the grain growth in 2D, reducing the computational cost. The initial average grain size of the thin films used in the experiments was around 10 nm and the sample thickness was 50 nm [12]. Therefore, it is reasonable that multiple grains could exist through the thickness, making our assumption of a columnar grain structure inaccurate. Modeling the grain growth behavior in 3D would provide a more accurate description of the growth behavior, but would also make the simulations very
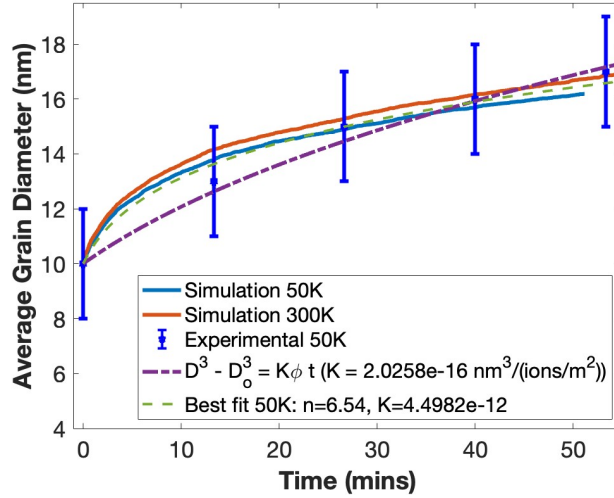
Fig. 10 Average grain diameter versus time at 50 K using a spike duration of 200 ps. Results at $T = 300$ K are shown for comparison. The experimental data from Yu et al. [12] are included for reference. Also shown are the analytical rate-theory prediction based on $D^n - D_0^n = K\phi t$ with $n = 3$, and the best-fit kinetic curve obtained for the 50 K data.

computationally expensive. However, 3D simulations could be carried out in the future to identify any significant differences in the behavior.

A second assumption made in our model is that no grain growth occurs between thermal spikes, so we can skip that time without missing any grain growth. This allows us to accelerate the simulations by artificially increasing the rate of a thermal spike. Our simulations shown in Fig. 8 demonstrate that no thermal grain growth occurs at 300 K, lending credence to this assumption. In addition, our results from Fig. 6a show that as long as we choose a small enough accelerated rate to ensure only one or two spikes occur during a time step, the impact on the average grain diameter with time is small.

Our final assumption is that the change in the GB mobility with temperature still follows an Arrhenius expression for temperatures above the melting temperature. When a thermal spike occurs within a material, it can experience localized melting that persists for a few picoseconds [38, 63]. Molecular dynamics simulations show that when the thermal spike overlaps a GB, the GB locally loses its character within the thermal spike as the material amorphizes but then reforms, having moved somewhat in that region [64]. These observations demonstrate that the temporary amorphization results in faster motion of the GB, but do not allow us to quantify how much faster it should be. Our assumption that it continues to follow the same Arrhenius expression is likely inaccurate, but there are no data available in the literature to provide better information about how the effective GB mobility

17

changes in the thermal spike. The calibration of the spike duration to the measured grain growth rates from the experiments helps to compensate for the inaccuracy of this assumption.

Our modeling approach is somewhat similar to that from Bufford et al. [11]. We both use a phase field grain growth model and stochastically introduce thermal spikes into the polycrystalline domain to accelerate the grain growth. However, the approach used to introduce the effect of the thermal spikes varies. They locally increase the GB mobility by an arbitrary amount and qualitatively compare the predicted grain growth to experimental grain growth in gold thin films. We directly represent the heat introduced into the material by the thermal spike and solve the heat equation to dissipate that heat through the material. Our approach allows a closer connection to the irradiation conditions and allows us to do a quantitative comparison with the experimental data, though some calibration is required. Another important difference between the two models is their results. In the model by Bufford et al. the irradiation results in somewhat faster grain growth than in thermal conditions. Our model predicts grain growth in conditions in which no thermal grain growth would normally occur. Thus, our model represents an important step forward in the mechanistic modeling of irradiation-assisted grain growth at the mesoscale.

Our simulations capture the grain growth behaviors shown in the experiments by Yu et al. [12]. Since our model is based on the hypothesized mechanism that irradiation-assisted grain growth is caused by thermal spikes, this supports this mechanism. This same mechanism is the basis of the mesoscale model developed by Buford et al. [11] and analytical model developed by Kaoumi et al. [7]. However, this does not eliminate other possible mechanisms for irradiation-assisted grain growth that are simply not dominant under the irradiation conditions used in the experiments by Yu et al. [12]. Thus, it would be interesting to investigate the impact of radiation on grain growth in conditions where thermal spikes would not occur. For example, experiments could be carried out using low energy irradiations which would add defects to the system but not cause a thermal spike.

The primary focus of this work is to develop a mechanistic model of irradiation-assisted grain grain in UO_2 so we can assess its impact on light water reactor fuel performance. Our simulations show rapid grain growth at first, even at low temperatures of 50 K and 300 K, but that the growth rate quickly slows down as the grain size increases. The average grain size quickly increases from the initial average grain size of 10 nm, but never gets higher than 15 or 20 nm. In the UO_2 experiments carried out by Yu et al. [12], the average grain size never increased above 35 nm for all temperatures and irradiation conditions, as shown in Fig. 1. Thus, from our results and from the experiments, it is clear
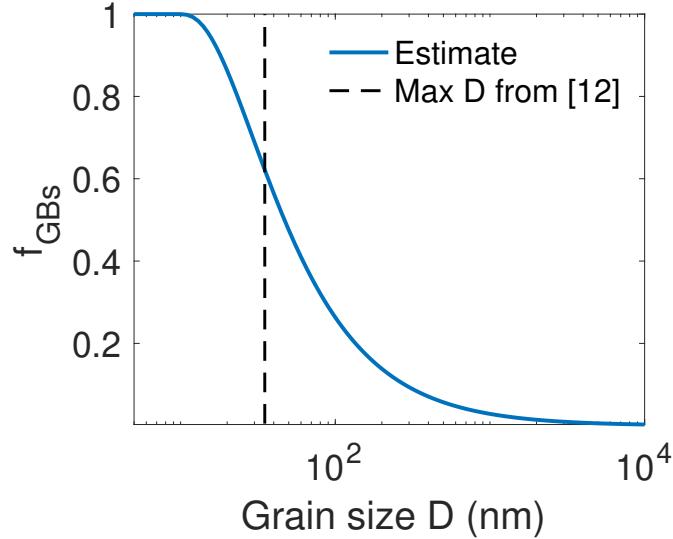
Fig. 11 Estimate of the fraction of thermal spikes that touch a GB calculated using Eq. (12). It is plotted for grain sizes ranging from 5 nm to 10 μm, assuming a spherical grain. The largest grain size reached in the experiments by Yu et al. [12] is shown with a dashed black line.

that the radiation enhancement is only significant for small grain sizes. This has also been observed in experiments showing irradiation-assisted grain growth in other materials [7, 8]. This occurs because as the grains grow, it is less likely that the thermal spike will overlap a GB, as illustrated in Fig. 7.

It is valuable to have a more quantitative approach for determining if irradiation-assisted grain growth needs to be considered in a given system. We can estimate this by considering a spherical grain of radius R, a thermal spike rate P_s, and a spike radius r_s. The total number of spikes that occur within this grain on average per unit time can be estimated by multiplying the rate by the grain volume to get $N_T = P_s 4/3\pi R^3$. In order for a thermal spike occurring within the grain to impact the GB, its center must lie within a distance $\leq r_s$ from the GB. Thus, the average number of spikes per unit time that occur within the grain interior but not touching the GB can be estimated as $N_{int} = P_s 4/3\pi(R - r_s)^3$. By dividing N_{int}/N_T and subtracting it from one, we can estimate the fraction of spikes that interact with the GB as

$$f_{GBs} = 1 - \frac{N_{int}}{N_T} = 1 - (1 - r_s/R)^3 \tag{12}$$

This estimated fraction for grain sizes $D = 2R$ ranging from 5 nm to 10 μm and $r_s = 4.84$ nm (see Table 1) is shown in Fig. 11.

The estimated fraction drops quickly once the grain size is greater than $2r_s$. At 35 nm, the largest average grain size seen in the samples irradiated by Yu et al. [12], the estimated fraction is around 60%.

However, the largest grains will be 1.5 to 2 times larger than the average, with fractions around 30%. So, the impact of the thermal spikes would be small for the larger grains that are growing. Thus, this estimate agrees reasonably well with the experimental data and our simulation results. The estimate predicts that at grain size of 10 μm, which is typical for fresh fuel, the fraction of thermal spikes that would contact a GB would be around 0.3%. Thus, irradiation-assisted grain growth can clearly be neglected for fresh fuel. High burnup structure (HBS) that can form during reactor operation, with an average grain size of hundreds of nm [65], would have fractions of thermal spikes impacting the GBs around 20% or lower, and so irradiation-assisted grain growth would also have little impact on HBS. From this, we conclude that irradiation-enhanced grain growth can be neglected when considering the performance of typical UO$_2$ fuel pellets.

6. Conclusion

We have developed a mesoscale model of irradiation-assisted grain growth using MARMOT. This model represents the impact of thermal spikes on grain growth by coupling a phase-field grain growth model with a heat conduction equation. Thermal spikes are represented by including a stochastic heat generation term and using the evolving temperature to determine the local grain boundary mobility. All of the parameters needed for the model were taken from the literature, except for the thermal spike duration. The model has been applied to simulate room temperature ion irradiations of UO$_2$ thin films, as documented in the work by Yu et al. [12]. Assuming a 100 ps spike duration results in significant grain growth at 300 K, even though thermally activated grain growth would not occur at this temperature. However, the growth rate was higher than that observed in the experiments. By fitting to the 300 K data, we determined that a spike duls ration of 200 ps provides the best match between simulation results and experiments. Using this spike duration, the results of the grain growth at 50 K compare well with data from Yu et al. [12]. These results provide evidence that thermal spikes are the primary mechanism for the irradiation-assisted grain growth observed by Yu et al. Our results also indicate that irradiation-assisted grain growth is only significant for grain sizes smaller than 35 nm; therefore, it does not need to be considered in fuel performance codes.

Credit Authorship Contribution Statement

Md Ali Muntaha: Investigation, Methodology, Analysis, Software, Writing original draft. **Larry Aagesen**: Conceptualization, Investigation, Supervision, Writing review and editing. **Michael R.**

Tonks: Conceptualization, Funding acquisition, Project administration, Supervision, Writing review and editing.

Declaration of Competing Interest

The authors declare that they have no known competing financial interests or personal relationships that could have appeared to influence the work reported in this paper.

Data Availability

The MOOSE input files used to generate the simulation results in this paper can be obtained from the authors upon reasonable request.

References

[1] W. W. Mullins, TwoDimensional Motion of Idealized Grain Boundaries, Journal of Applied Physics 27 (8) (1956) 900–904. doi:10.1063/1.1722511.

[2] G. Gottstein, L. S. Shvindlerman, Grain boundary migration in metals: thermodynamics, kinetics, applications, CRC press, 2009.

[3] M. Tonks, P.-C. Simon, J. Hirschhorn, Mechanistic grain growth model for fresh and irradiated UO_2 nuclear fuel, Journal of Nuclear Materials 543 (2021). doi:https://doi.org/10.1016/j.jnucmat.2020.152576.

[4] M. R. Tonks, Y. Zhang, X. Bai, P. C. Millett, Demonstrating the temperature gradient impact on grain growth in uo2 using the phase field method, Materials Research Letters 2 (1) (2014) 23–28. doi:10.1080/21663831.2013.849300.

[5] N. Moelans, F. Wendler, B. Nestler, Comparative study of two phase-field models for grain growth, Computational Materials Science 46 (2) (2009) 479–490. doi:https://doi.org/10.1016/j.commatsci.2009.03.037.

[6] F. A. Nichols, Theory of Grain Growth in Porous Compacts, Journal of Applied Physics 37 (13) (2004) 4599–4602. doi:10.1063/1.1708102.

[7] D. Kaoumi, A. Motta, R. Birtcher, A thermal spike model of grain growth under irradiation, Journal of Applied Physics 104 (7) (2008) 073525.

[8] D. Kaoumi, A. Motta, R. Birtcher, Grain growth in zrfe thin films during in situ ion irradiation in a tem, Nuclear Instruments and Methods in Physics Research Section B: Beam Interactions with Materials and Atoms 242 (1) (2006) 490–493, ion Beam Modification of Materials. doi:https://doi.org/10.1016/j.nimb.2005.08.158.

[9] Y. Zhang, W. Jiang, C. Wang, F. Namavar, P. D. Edmondson, Z. Zhu, F. Gao, J. Lian, W. J. Weber, Grain growth and phase stability of nanocrystalline cubic zirconia under ion irradiation, Phys. Rev. B 82 (2010) 184105. doi:10.1103/PhysRevB.82.184105.

[10] W. Voegeli, K. Albe, H. Hahn, Simulation of grain growth in nanocrystalline nickel induced by ion irradiation, Nuclear Instruments and Methods in Physics Research Section B: Beam Interactions with Materials and Atoms 202 (2003) 230–235, 6th International Conference on Computer Simulation of Radiation Effects in Solids. doi:https://doi.org/10.1016/S0168-583X(02)01862-1.

[11] D. Bufford, F. Abdeljawad, S. Foiles, K. Hattar, Unraveling irradiation induced grain growth with in situ transmission electron microscopy and coordinated modeling, Applied Physics Letters 107 (19) (2015) 191901.

[12] Z. Yu, X. Xu, W.-Y. Chen, Y. Sharma, X. Wang, A. Chen, C. J. Ulmer, A. T. Motta, In-situ irradiation-induced studies of grain growth kinetics of nanocrystalline uo2, Acta Materialia 231 (2022) 117856. doi:https://doi.org/10.1016/j.actamat.2022.117856.

[13] A. T. Motta, M. Tonks, In-situ ion irradiation to add irradiation assisted grain growth to the marmot tool, Tech. rep., Pennsylvania State Univ., University Park, PA (United States) (12 2021). doi:10.2172/1837940.
URL https://www.osti.gov/biblio/1837940

[14] D. Kaoumi, A. Motta, R. Birtcher, Grain growth in nanocrystalline metal thin films under in situ ion-beam irradiation, ASTM Special Technical Publication 1492 STP (2008) 206 218.

[15] J. Turnbull, The effect of grain size on the swelling and gas release properties of uo2 during irradiation, Journal of Nuclear Materials 50 (1) (1974) 62–68. doi:https://doi.org/10.1016/0022-3115(74)90061-0.

[16] K. Shrestha, T. Yao, J. Lian, D. Antonio, M. Sessim, M. R. Tonks, K. Gofryk, The grain-size effect on thermal conductivity of uranium dioxide, Journal of Applied Physics 126 (2019). doi:https://doi.org/10.1063/1.5116372.

[17] P. Toma, M. A. Muntaha, J. B. Harley, M. R. Tonks, Modeling fission gas release at the mesoscale using multiscale densenet regression with attention mechanism and inception blocks, Journal of Nuclear Materials 601 (2024) 155315. doi:https://doi.org/10.1016/j.jnucmat.2024.155315.

[18] M. A. Muntaha, S. Chatterjee, S. Blondel, L. Aagesen, D. Andersson, B. D. Wirth, M. R. Tonks, Impact of grain boundary and surface diffusion on predicted fission gas bubble behavior and release in uo2 fuel, Journal of Nuclear Materials 594 (2024) 155032. doi:https://doi.org/10.1016/j.jnucmat.2024.155032.

[19] B. Gong, D. Frazer, T. Yao, P. Hosemann, M. Tonks, J. Lian, Nano- and micro-indentation testing of sintered uo2 fuel pellets with controlled microstructure and stoichiometry, Journal of Nuclear Materials 516 (2019) 169–177. doi:https://doi.org/10.1016/j.jnucmat.2019.01.021.

[20] P. Robbe, T. Casey, C. Matthews, M. W. D. Cooper, S. Blondel, G. Pastore, D.-U. Kim, M. A. Muntaha, M. Tonks, B. Wirth, A. D. R. Andersson, H. Najm, Calibration of the diffusivity predictions of centipede using approximate bayesian computation and applications in nyx (engineering

scale) and xolotl-marmot (meso-scale) simulations, Tech. rep., Los Alamos National Lab. (LANL), Los Alamos, NM (United States) (9 2021). doi:10.2172/1845228.
URL https://www.osti.gov/biblio/1845228

[21] T. Watanabe, S. B. Sinnott, J. S. Tulenko, R. W. Grimes, P. K. Schelling, S. R. Phillpot, Thermal transport properties of uranium dioxide by molecular dynamics simulations, Journal of Nuclear Materials 375 (3) (2008) 388–396. doi:https://doi.org/10.1016/j.jnucmat.2008.01.016.

[22] D. Kim, S. Blondel, D. Bernholdt, P. Roth, F. Kong, D. Andersson, M. Tonks, B. Wirth, Modeling mesoscale fission gas behavior in UO_2 by directly coupling the phase field method to spatially resolved cluster dynamics, Materials Theory 6 7 (2022). doi:https://doi.org/10.1186/s41313-021-00030-8.

[23] G. Pastore, L. Luzzi, V. Di Marcello, P. Van Uffelen, Physics-based modelling of fission gas swelling and release in uo2 applied to integral fuel rod analysis, Nuclear Engineering and Design 256 (2013) 75–86. doi:https://doi.org/10.1016/j.nucengdes.2012.12.002.

[24] G. Pastore, L. Swiler, J. Hales, S. Novascone, D. Perez, B. Spencer, L. Luzzi, P. Van Uffelen, R. Williamson, Uncertainty and sensitivity analysis of fission gas behavior in engineering-scale fuel modeling, Journal of Nuclear Materials 456 (2015) 398–408. doi:https://doi.org/10.1016/j.jnucmat.2014.09.077.

[25] M. Oguma, Microstructure effects on fracture strength of uo2 fuel pellets, Journal of Nuclear Science and Technology 19 (12) (1982) 1005 1014. doi:10.1080/18811248.1982.9734249.

[26] S. Chatterjee, M. A. Muntaha, S. Blondel, D. Andersson, B. D. Wirth, M. R. Tonks, Influence of temperature, initial grain-boundary bubble density and grain structure on fission gas behaviour in uo$_2$: a 3d hybrid multiscale study (2025). arXiv:2511.20352.
URL https://arxiv.org/abs/2511.20352

[27] J. Ainscough, B. Oldfield, J. Ware, Isothermal grain growth kinetics in sintered uo2 pellets, Journal of Nuclear Materials 49 (2) (1973) 117–128. doi:https://doi.org/10.1016/0022-3115(73)90001-9.

[28] P. V. Nerikar, K. Rudman, T. G. Desai, D. Byler, C. Unal, K. J. McClellan, S. R. Phillpot, S. B. Sinnott, P. Peralta, B. P. Uberuaga, C. R. Stanek, Grain boundaries in uranium dioxide: Scanning electron microscopy experiments and atomistic simulations, Journal of the American Ceramic Society 94 (6) (2011) 1893–1900. doi:https://doi.org/10.1111/j.1551-2916.2010.04295.x.

[29] H. Sun, C. Deng, Direct quantification of solute effects on grain boundary motion by atomistic simulations, Computational Materials Science 93 (2014) 137–143. doi:https://doi.org/10.1016/j.commatsci.2014.06.040.

[30] K. Ahmed, J. Pakarinen, T. Allen, A. El-Azab, Phase field simulation of grain growth in porous uranium dioxide, Journal of Nuclear Materials 446 (1) (2014) 90–99. doi:https://doi.org/10.1016/j.jnucmat.2013.11.036.

[31] K. Ahmed, M. Tonks, Y. Zhang, B. Biner, A. El-Azab, Particle-grain boundary interactions: A phase field study, Computational Materials Science 134 (2017) 25–37. doi:https://doi.org/10.1016/j.commatsci.2017.03.025.

[32] Y. Guo, Z. Liu, Q. Huang, C.-T. Lin, S. Du, Abnormal grain growth of uo2 with pores in the final stage of sintering: A phase field study, Computational Materials Science 145 (2018) 24–34. doi:https://doi.org/10.1016/j.commatsci.2017.12.057.

[33] H. Hallberg, Y. Zhu, Stability of grain boundary texture during isothermal grain growth in uo2 considering anisotropic grain boundary properties, Journal of Nuclear Materials 465 (2015) 664–673. doi:https://doi.org/10.1016/j.jnucmat.2015.06.052.

[34] M. R. Tonks, Y. Zhang, A. Butterfield, X.-M. Bai, Development of a grain boundary pinning model that considers particle size distribution using the phase field method, Modelling and Simulation in Materials Science and Engineering 23 (4) (2015) 045009. doi:10.1088/0965-0393/23/4/045009.

[35] R. Stoller, M. Toloczko, G. Was, A. Certain, S. Dwaraknath, F. Garner, On the use of srim for computing radiation damage exposure, Nuclear Instruments and Methods in Physics Research Section B: Beam Interactions with Materials and Atoms 310 (2013) 75–80. doi:https://doi.org/10.1016/j.nimb.2013.05.008.

[36] N. Moelans, B. Blanpain, P. Wollants, Quantitative analysis of grain boundary properties in a generalized phase field model for grain growth in anisotropic systems, Physical Review B 78 (2) (2008) 024113.

[37] M. R. Tonks, P.-C. A. Simon, J. Hirschhorn, Mechanistic grain growth model for fresh and irradiated uo2 nuclear fuel, Journal of Nuclear Materials 543 (2021) 152576.

[38] T. D. De La Rubia, R. S. Averback, R. Benedek, W. King, Role of thermal spikes in energetic displacement cascades, Physical review letters 59 (17) (1987) 1930.

[39] C. Ulmer, W.-Y. Chen, D. Wolfe, A. Motta, In-situ ion irradiation induced grain growth in nanocrystalline ceria, Journal of Nuclear Materials 545 (2021) 152688. doi:https://doi.org/10.1016/j.jnucmat.2020.152688.

[40] A. E. Stuchbery, E. Bezakova, Thermal-spike lifetime from picosecond-duration preequilibrium effects in hyperfine magnetic fields following ion implantation, Phys. Rev. Lett. 82 (1999) 3637–3640. doi:10.1103/PhysRevLett.82.3637.

[41] S. Heredia-Avalos, C. Denton, J. Moreno-Marín, E. Martinez, M. Caturla, Collision cascade effects near an edge dislocation dipole in alpha-fe: Induced dislocation mobility and enhanced defect clustering, Journal of Nuclear Materials 543 (2021) 152459. doi:https://doi.org/10.1016/j.jnucmat.2020.152459.

[42] V. Baranov, Y. Devyatko, A. Tenishev, New method for determining the temperature dependence of the thermal conductivity coefficient of dielectrics in a pulse experiment, Inorg. Mater. Appl. Res. 1 (2010) 167173doi:https://doi.org/10.1134/S2075113310020164.

[43] R. Gibby, The effect of plutonium content on the thermal conductivity of (u, pu)o2 solid solutions, Journal of Nuclear Materials 38 (2) (1971) 163–177. doi:https://doi.org/10.1016/0022-3115(71)90040-7.

[44] T. G. GODFREY, W. FULKERSON, T. G. KOLLIE, J. P. MOORE, D. L. McELROY, Thermal conductivity of uranium dioxide from -57ř to 1100řc by a radial heat flow technique, Journal of the American Ceramic Society 48 (6) (1965) 297–305. doi:https://doi.org/10.1111/j.1151-2916.1965.tb14745.x.

[45] H. Kim, M. H. Kim, M. Kaviany, Lattice thermal conductivity of UO2 using ab-initio and classical molecular dynamics, Journal of Applied Physics 115 (12) (2014) 123510. doi:10.1063/1.4869669.

[46] W. D. KINGERY, J. FRANCL, R. L. COBLE, T. VASILOS, Thermal conductivity: X, data for several pure oxide materials corrected to zero porosity, Journal of the American Ceramic Society 37 (2) (1954) 107–110. doi:https://doi.org/10.1111/j.1551-2916.1954.tb20109.x.

[47] J. L. Bates, High-temperature thermal conductivity of round robin uranium dioxide., Tech. rep., Battelle Pacific Northwest Lab. (PNNL), Richland, WA (United States) (1 1970). doi:10.2172/4084378.
URL https://www.osti.gov/biblio/4084378

[48] M. Sheindlin, D. Staicu, C. Ronchi, L. Game-Arnaud, B. Remy, A. Degiovanni, Experimental determination of the thermal conductivity of liquid UO2 near the melting point, Journal of Applied Physics 101 (9) (2007) 093508. doi:10.1063/1.2721091.

[49] J. W. L. Pang, W. J. L. Buyers, A. Chernatynskiy, M. D. Lumsden, B. C. Larson, S. R. Phillpot, Phonon lifetime investigation of anharmonicity and thermal conductivity of uo$_2$ by neutron scattering and theory, Phys. Rev. Lett. 110 (2013) 157401. doi:10.1103/PhysRevLett.110.157401.

[50] B.-T. Wang, J.-J. Zheng, X. Qu, W.-D. Li, P. Zhang, Thermal conductivity of uo2 and puo2 from first-principles, Journal of Alloys and Compounds 628 (2015) 267–271. doi:https://doi.org/10.1016/j.jallcom.2014.12.204.

[51] C. Ronchi, M. Sheindlin, M. Musella, G. J. Hyland, Thermal conductivity of uranium dioxide up to 2900 K from simultaneous measurement of the heat capacity and thermal diffusivity, Journal of Applied Physics 85 (2) (1999) 776–789. doi:10.1063/1.369159.

[52] J. Fink, Thermophysical properties of uranium dioxide, Journal of Nuclear Materials 279 (1) (2000) 1–18. doi:https://doi.org/10.1016/S0022-3115(99)00273-1.

[53] T. Engel, The heat capacities of al2o3, uo2 and puo2 from 300 to 1100 řk, Journal of Nuclear Materials 31 (2) (1969) 211–214. doi:https://doi.org/10.1016/0022-3115(69)90194-9.

[54] P. Goel, N. Choudhury, S. Chaplot, Atomistic modeling of the vibrational and thermodynamic properties of uranium dioxide, uo2, Journal of Nuclear Materials 377 (3) (2008) 438–443. doi:https://doi.org/10.1016/j.jnucmat.2008.03.020.

[55] F. Grønvold, N. J. Kveseth, A. Sveen, J. Tichý, Thermodynamics of the uo2+x phase i. heat capacities of uo2.017 and uo2.254 from 300 to 1000 k and electronic contributions, The Journal of Chemical Thermodynamics 2 (5) (1970) 665–679. doi:https://doi.org/10.1016/0021-9614(70)90042-X.

[56] J. J. Huntzicker, E. F. Westrum, The magnetic transition, heat capacity, and thermodynamic properties of uranium dioxide from 5 to 350 k, The Journal of Chemical Thermodynamics 3 (1) (1971) 61–76. doi:https://doi.org/10.1016/S0021-9614(71)80067-8.

[57] H. Inaba, K. Naito, M. Oguma, Heat capacity measurement of $u_{1-y}gd_yo_2$ from 310 to 1500 k, Journal of Nuclear Materials 149 (3) (1987) 341–348. doi:https://doi.org/10.1016/0022-3115(87)90536-8.

[58] Y. Takahashi, M. Asou, High-temperature heat-capacity measurements on (u, gd)o2 by drop calorimetry and dsc, Journal of Nuclear Materials 201 (1993) 108–114. doi:https://doi.org/10.1016/0022-3115(93)90164-T.

[59] Y. Yun, D. Legut, P. M. Oppeneer, Phonon spectrum, thermal expansion and heat capacity of uo2 from first-principles, Journal of Nuclear Materials 426 (1) (2012) 109–114. doi:https://doi.org/10.1016/j.jnucmat.2012.03.017.

[60] M. R. Tonks, D. Gaston, P. C. Millett, D. Andrs, P. Talbot, An object-oriented finite element framework for multiphysics phase field simulations, Computational Materials Science 51 (1) (2012) 20–29.

[61] C. J. Permann, D. R. Gaston, D. Andrš, R. W. Carlsen, F. Kong, A. D. Lindsay, J. M. Miller, J. W. Peterson, A. E. Slaughter, R. H. Stogner, et al., Moose: Enabling massively parallel multiphysics simulation, SoftwareX 11 (2020) 100430.

[62] C. J. Permann, M. R. Tonks, B. Fromm, D. R. Gaston, Order parameter re-mapping algorithm for 3d phase field model of grain growth using fem, Computational Materials Science 115 (2016) 18–25. doi:https://doi.org/10.1016/j.commatsci.2015.12.042.

[63] A. Meldrum, S. Zinkle, L. Boatner, R. C. Ewing, A transient liquid-like phase in the displacement cascades of zircon, hafnon and thorite, Nature 395 (6697) (1998) 56–58.

[64] A. Kedharnath, R. Kapoor, A. Sarkar, Atomistic simulation of interaction of collision cascade with different types of grain boundaries in α-fe, Journal of Nuclear Materials 523 (2019) 444–457.

[65] V. V. Rondinella, T. Wiss, The high burn-up structure in nuclear fuel, Materials today 13 (12) (2010) 24–32.

[66] S. J. Parker, M. W. Anderson, Nuclear science user facilities high performance computing: Fy 2022 annual report, Tech. rep., Idaho National Lab. (INL), Idaho Falls, ID (United States) (3 2023).
URL https://www.osti.gov/biblio/1964106

[67] S. J. Parker, B. H. Jensen, B. F. Rothwell, M. W. Anderson, J. L. Yancey, Nuclear science user facilities high performance computing: Fy 2024 annual report, Tech. rep., Idaho National Lab. (INL), Idaho Falls, ID (United States) (3 2025).
URL `https://www.osti.gov/biblio/2572900`